Image Processing of Illuminated Ellipsoid

Daniele Mortari[1],
Texas A&M University, College Station, TX 77843

Christopher N. D'Souza,[2] and Renato Zanetti[3]
NASA Johnson Space Center, Houston, TX, 77058

This study introduces novel algorithms and the underlying mathematics to process pictures of planetary illuminated bodies and use them for navigation purposes. The goal is to accurately estimate the observer-to-body relative position in inertial coordinates. The main motivation is to provide autonomous navigation capabilities to spacecrafts by observing a planet or a moon. This is needed, for example, in human-rated vehicles in order to provide navigation capabilities in a loss of communications scenario. The algorithm is derived for the general case of a triaxial ellipsoid which is observed bounded by an elliptical cone. The orientation of the elliptical cone reference frame is obtained by eigenanalysis and the offset between the elliptical cone axis and the body center direction as well as the equation of the terminator are quantified. The main contribution of this paper is in the image processing approach adopted to derive centroid and distance to the body. This is done by selecting a set of pixels around the body limb and modeling the smooth limb transition using two-dimensional circular and elliptical sigmoid functions. More accurate estimates of centroid and distance are then obtained by iterative nonlinear least-squares using these models. Sensitivity analysis is performed and numerical examples using a real Moon picture taken from Earth is provided to clarify the image processing steps and to validate the proposed theory.

---

[1] Professor, 746C H.R. Bright Bldg., Aerospace Engineering, AIAA Associate Fellow. E-mail: mortari@tamu.edu
[2] GN&C Autonomous Flight Systems Engineer, Aeroscience and Flight Mechanics Division. AIAA Associate Fellow.
[3] GN&C Autonomous Flight Systems Engineer, Aeroscience and Flight Mechanics Division, AIAA Associate Fellow.

<div align="center">**Nomenclature**</div>

J — Ellipsoid diagonal matrix

a', b' — Observed ellipse semi-axes

$\boldsymbol{p}$ — Observer position vector (J2000)

γ_{off} — Observed body center offset angle

$\hat{\boldsymbol{v}}$ — Unit vector

r_i — Row index of the generic pixel

c_i — Column index of the generic pixel

f — Camera focal length (mm)

r_m — Imager Moon radius (mm)

R_m — Moon radius (km)

D_m — Observer to Moon distance (km)

k — Sigmoid smoothing factor

$\mathcal{J}$ — Jacobian (sigmoid functions)

$\hat{\boldsymbol{v}}$ — Unit vector

σ_x — Standard deviation of x

<div align="center">**I.   Introduction**</div>

In cislunar space [1] the position of a spacecraft is usually estimated by communicating with Earth tracking stations while the orientation is obtained onboard using attitude sensors. In order to have a fault tolerant system, it is often desired to augment the spacecraft with a backup autonomous navigation system to be used in case of communications loss (permanent or temporarily). The approach used in this paper is to use a visible camera as a "positioning sensor" by observing the closest celestial body (e.g, Moon or Earth) [2–4]. From the images the observer-to-body vector is derived from the apparent size and location of the celestial body on the sensor imager. Subsequently, a sequence of these vectors can be used to estimate the trajectory by filtering techniques such as iterative batch least-squares or extended Kalman Filter.

<div align="center">2</div>

The Vision-based Navigation (VisNav) is an old problem in aerospace engineering [5]. Reference [6] contains a detailed literature review on the traditional approaches taken to solve the VisNav problem. In the 1960s (see Ref. [7]) a solution to this problem (first optical navigation) consisted of using visible cameras taking pictures of observed illuminated bodies surrounded by a set of catalogued reference stars. All six Voyager flybys of the outer planets [8, 9] and Cassini's orbital operations at Saturn [10] adopted this approach. In particular, Refs. [8, 9] presented the optical observables for the Voyager II Uranus and Neptune approaches and encounters. Using two distinct cameras (because of the different magnitude threshold settings for stars and illuminated body) the angular distances between body (considered as a circle) and stars were measured.

Later various attempts were performed to estimate the navigation measurements by fitting the observed body by circles and ellipses. To perform this task the problem of selecting the limb pixels must be first solved. A Canny edge detection algorithm to identify the Moon limb was adopted in Ref. [11] and then, using Levenberg-Marquardt ellipse least-squares algorithm, the limb pixels that are considered potential false were removed. The remaining pixels were then used to estimate the line-of-sight vector to the centroid of the observed object. Different and (sometime) more accurate limb detection algorithms as well as optimization techniques were proposed. Among these existing approaches we can mention Laplacian, Sobel, Roberts and Prewitt operators, Gaussian derivatives and Gabor filters. All these methods are certainly more accurate to discriminate limb pixels but computationally more intensive. Various curve fitting approaches (using circles and ellipses) have also been proposed. In Refs. [6, 12] a thorough comparison analysis among various existing mathematical techniques to best estimate circles and ellipses is presented. In general, these techniques can be classified in two distinct classes depending if the error is defined as geometrical or algebraic. It is important to outline that all the ellipse regression techniques are usually more accurate to estimate center and semi-axes (four parameters) and less accurate to estimate the ellipse orientation (ellipse fifth parameter), especially if the ellipse eccentricity is small (as for the Earth). However, to obtain accurate estimation the ellipse orientation is needed to correct the offset between body center and ellipse center directions.

The approach proposed in this study attacks the problem in a different way (See Ref. [13]).

First, it takes into consideration a practical aspect (sophisticated and/or computationally intensive approaches to identify limb pixels or to perform optimization cannot be used in limited onboard computers) and second –more importantly– the following pragmatic fact. The limb of an illuminated body consists of a smooth (and not discontinuous) transition between the bright illuminated part of the body and the dark of the background sky. This smooth transition is more evident for a planet with atmosphere. However, even if the observed body has no atmosphere and a perfect geometric limb, the limb transition would still appear smooth because cameras focusing is never perfect and because of pixelation of photometric cameras. For this reason, instead of adopting a one-dimensional model (ellipse), a two-dimensional model (surface) to describe the body limb transition is here proposed and analyzed. This two-dimensional model (circular or elliptical sigmoid functions) and the nonlinear least-squares to estimate centroid and distance are the main contribution of this study.

The main overall characteristics of the proposed methods are:

1. it uses just one visible camera and does not use observed stars as the attitude information is assumed known and provided by the onboard star tracker;

2. it is suitable for small on-board computers as it does not require computationally intensive pixel selection or optimization techniques, and

3. it uses a two-dimensional model to describe the smooth limb transition (to increase the estimation accuracy) and a standard nonlinear least-squares to estimate centroid and distance.

The next section summarizes the algorithm presented in this work, followed by a section introducing the mathematical background for the limb and terminator identification. Subsequently, the two-dimensional *sigmoid functions*, which are used for high precision body center and radius estimation, are introduced. Lastly, a test performed using a real Moon image (as taken from Earth) is discussed in detail to show the algorithm performance.

Even though the Moon is modeled as a sphere and the Earth as a spheroid, the theory of body observation and terminator equations are developed for the general case of a triaxial ellipsoid. The proposed approach is applied to real pictures of the Moon taken from Earth. The noise presence is

4

mainly due to the atmosphere.

II. Image processing summary

```
┌──────────────────────┐     ┌──────────────────────┐     ┌──────────────────────┐
│ SPICE (Moon vector and│····▶│ Read picture, time,   │◀····│ Position propagation  │
│ illumination geometry)│     │ camera parameters.    │     │ (EKF)                 │
└──────────────────────┘     └──────────────────────┘     └──────────────────────┘
                                        │                              ▲
                                        ▼                              ·
┌──────────────────────┐     ┌──────────────────────┐     ┌──────────────────────┐
│ Eigenanalysis (axis of│◀────│ Box selection and     │     │ Position Estimation   │
│ symmetry estimation)  │     │ binary conversion     │     │                       │
└──────────────────────┘     └──────────────────────┘     └──────────────────────┘
         │                                                            ▲
         ▼                                                            │
┌──────────────────────┐     ┌──────────────────────┐     ┌──────────────────────┐
│ Edge pixel selection  │     │ Attitude              │····▶│ Observer to Moon      │
│ and initial estimation│     │ (from star tracker)   │     │ vector (J2000)        │
└──────────────────────┘     └──────────────────────┘     └──────────────────────┘
         │                                                            ▲
         ▼                                                            │
┌──────────────────────┐     ┌──────────────────────┐     ┌──────────────────────┐
│ Selection of pixels   │────▶│ Least-squares by circular│──▶│ Observer to Moon    │
│ around body edge      │     │ sigmoid function      │     │ vector (body frame)   │
└──────────────────────┘     └──────────────────────┘     └──────────────────────┘
```
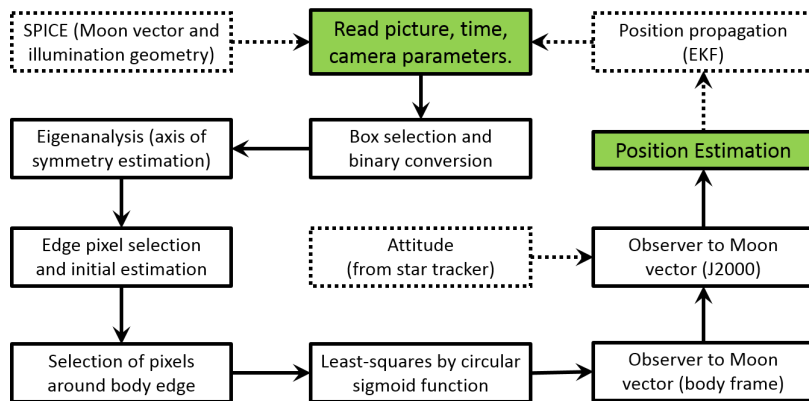
Fig. 1 Moon Image Processing Flowchart

The various steps of the proposed Moon image processing are shown in Fig. 1. The rationale of each step is summarized in the following:

1. Input data are: the image taken by the camera, the time stamp, the camera parameters, and the camera attitude (for example deduced from a star tracker). Using the time stamp, the position vector of the Moon in J2000 ($\boldsymbol{r}_m$) is computed using SPICE [14]. In addition, a rough position estimation (propagated by the EKF at the time stamp) is used to estimate an illumination parameter: the expected fraction of the illuminated area with respect to the total body area. This parameter allows to discriminate the four cases of: a) full, b) gibbous c) crescent, and d) new Moon.

2. The image is converted in binary format (black and white). A sub-window is identified where most of the illuminated Moon is. Then, the centroid of the illuminated area is computed (it belongs to the axis of symmetry of the illuminated area) and the eigenanalysis of the "inertia tensor" of the sub-window is performed to estimate the axis of symmetry of the illuminated area. This is the axis associated with the maximum eigenvalue.

3. Several parallel lines, including the axis of symmetry, are plotted in the binary images (see Fig. 7). These lines intersect the illuminated area in two sets of points. One set of points

belongs to the Moon limb, the other to the terminator. Two least-squares estimates of circle are performed using these two sets of points. This allows to discriminate the set of points belonging to the bright limb because of smaller residuals and radius estimate closer to the expected one provided by propagation (EKF). The circle least-squares approach adopted is the Taubin's SVD-based approach [15], consisting of Moon centroid and radius, $\hat{R}_m$.

4. Using this initial estimate a selection of pixels around the illuminated body limb is obtained. These pixels are those between two radii, $\hat{R}_m - \delta R_m$ and $\hat{R}_m + \delta R_m$, where δR_m is a few pixels.

5. The initial estimate and these selected pixels around the illuminated Moon limb are then used to perform a more accurate nonlinear least-squares estimation using circular sigmoid function. The accurate estimated Moon radius allows the estimation of the observer-to-Moon distance. This distance multiplied by the centroid direction is the observer-to-Moon vector in the camera reference frame, $\boldsymbol{r}_{om}$. The Earth image processing uses the elliptical sigmoid function and the Earth center offset as well as the distance estimation is performed by iterative process. This is described in the Earth image processing section.

6. Using the attitude provided by a star tracker, this vector is transformed in the inertial (J2000) reference frame.

7. Finally, the observer position estimate is $\boldsymbol{r}_o = \boldsymbol{r}_m - \boldsymbol{r}_{om}$.

The process summarized above is discussed in further details in the following sections.

III. Observed triaxial ellipsoid

The canonical equation of a triaxial ellipsoid in the body-centered body-fixed coordinates is

$$\boldsymbol{x}^{\mathrm{T}} J \boldsymbol{x} = 1, \tag{1}$$

where $\boldsymbol{x}$ is a vector belonging to the ellipsoid surface, $J = \mathrm{diag}\{\, a^{-2},\ b^{-2},\ c^{-2}\,\}$, and a, b, and c, are the three semi-principal axes of the ellipsoid. Indicating by $\boldsymbol{p}$ the position vector of the observer the equation of the observed ellipsoid limb is obtained as described in Ref. [13], as a quadratic equation

in the direction ($\hat{\boldsymbol{v}}$) tangent to the ellipsoid,

$$\hat{\boldsymbol{v}}^{\mathrm{T}} M \hat{\boldsymbol{v}} = 0, \tag{2}$$

where M is a symmetric matrix whose expression is

$$M = J\boldsymbol{p}\boldsymbol{p}^{\mathrm{T}} J - (\boldsymbol{p}^{\mathrm{T}} J\boldsymbol{p} - 1)J.$$

Since M is symmetric ($M = M^{\mathrm{T}}$) its eigenvector matrix is orthogonal. This means, $M = C_{ie} \Lambda C_{ie}^{\mathrm{T}}$, where Λ is the diagonal eigenvalue matrix and C_{ie} is an orthogonal transformation matrix. Replacing M in Eq. (2) by $C_{ie} \Lambda C_{ie}^{\mathrm{T}}$ we obtain,

$$(\hat{\boldsymbol{v}}^{\mathrm{T}} C_{ie}) \Lambda (C_{ie}^{\mathrm{T}} \hat{\boldsymbol{v}}) = \hat{\boldsymbol{w}}^{\mathrm{T}} \Lambda \hat{\boldsymbol{w}} = 0, \tag{3}$$

where $\hat{\boldsymbol{w}} = C_{ie}^{\mathrm{T}} \hat{\boldsymbol{v}}$ is a rotated unit vector and C_{ie} is the matrix moving from an elliptical cone reference to inertial. Equation (3) can be written is a scalar way,

$$\lambda_1 w_1^2 + \lambda_2 w_2^2 + \lambda_3 w_3^2 = 0, \tag{4}$$

where λ_1, λ_2, and λ_3, are the eigenvalues of M, and w_1, w_2, and w_3 are the three components of the unit vector $\hat{\boldsymbol{w}}$.

In order for Eq. (4) to admit solutions, the three eigenvalues cannot have the same sign. Two cases are possible

1. one eigenvalue is positive (λ_p) and two are negative (λ_{n1} and λ_{n2}) or

2. two eigenvalues are positive (λ_{p1} and λ_{p2}) and one is negative (λ_n)

The first case implies $\det(M) = \det(\Lambda) > 0$ while the second case $\det(M) < 0$. Next subsection proves $\det(M) > 0$ is true.

A. Eigenvalues proof

Let's apply Sylvester's determinant theorem,

$$\det(X Y + Z) = \det(Z) \det(I_{n \times n} + Y Z^{-1} X),$$

to matrix M, where

$$X \equiv J \boldsymbol{p}\boldsymbol{p}^{\mathrm{T}}, \qquad Y \equiv J, \qquad \text{and} \qquad Z \equiv (1 - \boldsymbol{p}^{\mathrm{T}} J\boldsymbol{p})J.$$

7

This means,

$$\det(M) = (1 - \boldsymbol{p}^{\mathrm{T}} J \boldsymbol{p})^3 \det(J) \det(I_{3\times 3} + J(1 - \boldsymbol{p}^{\mathrm{T}} J \boldsymbol{p})^{-1} J^{-1} J \boldsymbol{p} \boldsymbol{p}^{\mathrm{T}}),$$

that can be written as,

$$\det(M) = (1 - \boldsymbol{p}^{\mathrm{T}} J \boldsymbol{p})^3 \det(J) \det(I_{3\times 3} + (1 - \boldsymbol{p}^{\mathrm{T}} J \boldsymbol{p})^{-1} J \boldsymbol{p} \boldsymbol{p}^{\mathrm{T}}). \tag{5}$$

Now, let's apply again Sylvester's determinant theorem with

$$X \equiv I_{3\times 3}, \qquad Y \equiv (1 - \boldsymbol{p}^{\mathrm{T}} J \boldsymbol{p})^{-1} J \boldsymbol{p}, \qquad \text{and} \qquad Z \equiv \boldsymbol{p}^{\mathrm{T}}.$$

Then, Eq. (5) becomes

$$\det(M) = (1 - \boldsymbol{p}^{\mathrm{T}} J \boldsymbol{p})^3 \det(J) \left[1 + (1 - \boldsymbol{p}^{\mathrm{T}} J \boldsymbol{p})^{-1} \boldsymbol{p}^{\mathrm{T}} J \boldsymbol{p} \right]. \tag{6}$$

By setting $\gamma = \boldsymbol{p}^{\mathrm{T}} J \boldsymbol{p} > 1$, Eq. (6) becomes

$$\det(M) = (1 - \gamma)^3 \det(J) \left(1 + \frac{\gamma}{1 - \gamma} \right) = (1 - \gamma)^3 \det(J) \frac{1 - \gamma + \gamma}{1 - \gamma} = (1 - \gamma)^2 \det(J) > 0,$$

proving that $\det(M) > 0$. Hence, matrix M has one eigenvalue positive (λ_p) and two negative (λ_{n1} and λ_{n2}).

B.   Observed semi-axes and ratio

Let us consider $\lambda_p = \lambda_3 > 0$ and $\lambda_1, \lambda_2 < 0$. By setting $|\lambda_i| = \xi_i^{-2}$, Eq. (4) becomes

$$\frac{w_1^2}{\xi_1^2} + \frac{w_2^2}{\xi_2^2} = \frac{w_3^2}{\xi_3^2}, \tag{7}$$

which is the equation of an elliptic cone with axis along $\hat{\boldsymbol{w}}_3 = \{0,\ 0,\ 1\}^{\mathrm{T}}$ (axis associated with the positive eigenvalue). Since $\hat{\boldsymbol{w}}$ is a unit vector then the elliptic cone, given in Eq. (7), intersects the unit radius sphere

$$w_1^2 + w_2^2 + w_3^2 = 1.$$

Substituting, $w_3^2 = 1 - w_1^2 - w_2^2$, in Eq. (7) we obtain the equation of the observed ellipse,

$$w_1^2 \left(1 + \xi_3^2/\xi_1^2 \right) + w_2^2 \left(1 + \xi_3^2/\xi_2^2 \right) = 1,$$

The semi-axes of this ellipse are

$$a' = \sqrt{\frac{\xi_1^2}{\xi_1^2 + \xi_3^2}} < 1 \qquad \text{and} \qquad b' = \sqrt{\frac{\xi_2^2}{\xi_2^2 + \xi_3^2}} < 1, \tag{8}$$

and the ratio of the semi-axes is

$$\rho = \frac{b'}{a'} = \sqrt{\frac{\xi_2^2(\xi_1^2 + \xi_3^2)}{\xi_1^2(\xi_2^2 + \xi_3^2)}}. \tag{9}$$

In conclusion, a triaxial ellipsoid is observed as an ellipse. However, the direction to the center of the observed ellipse for a generic ellipsoid does not coincide with the direction to the center of the ellipsoid. This deviation and how to apply the associated correction (which is important when the observed body is the Earth) is explained and quantified in the following subsection.

IV. Earth image processing

The Earth image processing follows the flowchart provided in Fig. 1, where the elliptical sigmoid function is adopted. In addition, the center offset (γ_{off}), semi-axis ratio (ρ), and the Earth distance are all computed by the iterative procedure shown in Fig. 2. This iterative procedure does not require more than 2 iterations to converge and starts from a position estimate, $\boldsymbol{p}_0 = E\{\boldsymbol{p}\} = \{x_p,\ y_p,\ z_p\}^{\mathrm{T}}$ (dashed box).
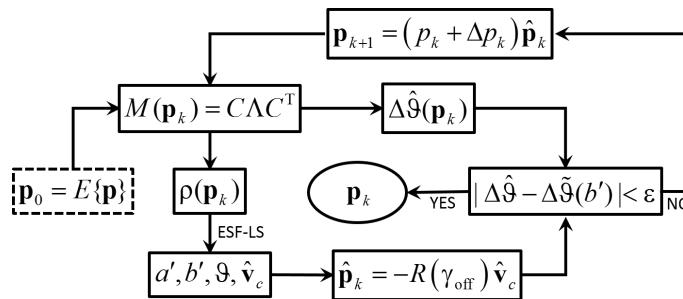
Fig. 2 Flowchart of position estimation for Earth image processing

The Earth center offset correction, γ_{off}, and the observed semi-axis ratio, ρ, are function of the observer distance and latitude, only. Figure 3 shows the values of γ_{off} (in arcsec) for the whole positive latitudes (for negative latitudes values - from south pole to equator - the γ_{off} values are negative) and from GEO to Earth-Moon for distances.

The γ_{off} corrections are small with small variations with respect to the initial position estimate accuracy (even with error of 1,000 km). Usually, the predicted position $\boldsymbol{p}_0 = E\{\boldsymbol{p}\}$, is obtained
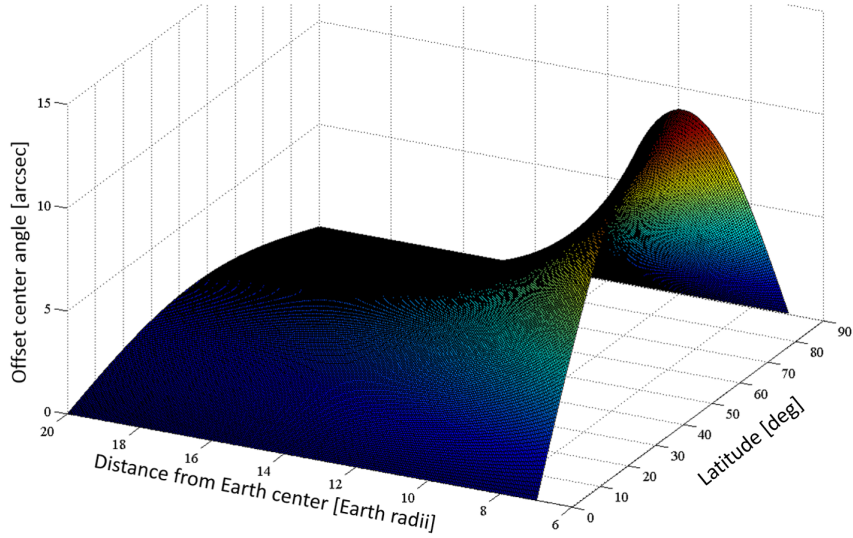
9

Fig. 3 Offset center correction (γ_{off}) surface

using EKF propagation to the current time and the expected EKF propagation precision (for Orion is about 10 km at 3σ). The observed semi-axis ratio, ρ, has also small variations with respect to the initial position estimate accuracy. In particular, ρ is computed from the eigenanalysis of matrix $M(\boldsymbol{p})$ using Eq. (9). The Earth center offset correction is just a rigid rotation of the direction $\hat{\boldsymbol{v}}_c^{\text{T}} = C_{ie}\{0,\ 0,\ 1\}^{\text{T}}$ by the angle γ_{off} about an axis orthogonal to $\hat{\boldsymbol{v}}_c$ and to the Earth spin axis direction, $\{0,\ 0,\ 1\}^{\text{T}}$.
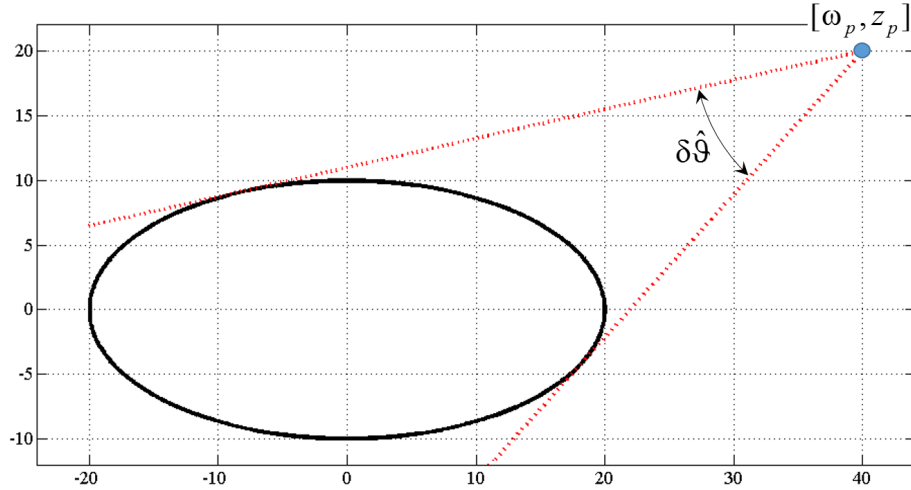
Fig. 4 Observed semi-minor angle geometry

With reference to Fig. 4, consider the equation of the Earth ellipse in the meridian plane of the

10

observer position,

$$\frac{\rho^2}{R_e^2} + \frac{z^2}{R_p^2} = 1 \qquad \text{where} \qquad \rho^2 = x^2 + y^2,$$

where R_p and R_e are the Earth's polar and equatorial radii (plus atmosphere altitude), respectively.

The line passing through the observer position (coordinates $[\rho_p, z_p]$) is

$$z = m(\rho - \rho_p) + z_p.$$

With simple derivations, the two slope values of the lines tangent to the ellipse are

$$m_{1,2} = \frac{\rho_p z_p \pm \sqrt{\rho_p^2 R_p^2 + z_p^2 R_e^2 - R_e^2 R_p^2}}{\rho_p^2 - R_e^2} = \tan \vartheta_{1,2}.$$

The angle between these two slopes, $\delta\hat{\vartheta}$ (see Fig. 4), must be the same as the angle between the two directions pointing to the limb of the minor axis of the observed ellipse in camera reference frame. This angle satisfies

$$\sin\left(\frac{\delta\tilde{\vartheta}}{2}\right) = b'.$$

If $\delta\hat{\vartheta} > \delta\tilde{\vartheta}$, then the estimated distance, $|\boldsymbol{p}_0|$, is too short; if $\delta\hat{\vartheta} < \delta\tilde{\vartheta}$, too long. The value of $\boldsymbol{p}_0$ is then modified by Δp until the convergence,

$$|\delta\hat{\vartheta} > \delta\tilde{\vartheta}| < \varepsilon,$$

where ε is a prescribed tolerance, is obtained. The variation Δp, which can be derived from simple geometric consideration from Fig. 4, has the expression

$$\Delta p = -R \frac{\cos(\delta\vartheta/2)}{2\sin^2(\delta\vartheta/2)} (\delta\hat{\vartheta} - \delta\tilde{\vartheta}),$$

until convergence is achieved, where $\delta\vartheta$ can be $\delta\hat{\vartheta}$ or $\delta\tilde{\vartheta}$ and R can be R_e or R_p. If convergence is not achieved, the position vector is updated by

$$\boldsymbol{p}_{k+1} = (p_k + \Delta p_k)\, \hat{\boldsymbol{p}}_k,$$

where $\hat{\boldsymbol{p}}_k$ is the unit vector pointing to the Earth center, corrected by rotating the direction pointing to the observed ellipse center by the offset angle, γ_{off}. The process is then iterated. This procedure is summarized in the flowchart of Fig. 2.

A. Principal axes of illuminated area

The image is converted into binary by choosing a threshold greytone value $\mathcal{G}_t$, dependent upon the maximum and minimum values contained in the image. A reasonable estimation for $\mathcal{G}_t$ is

$$\mathcal{G}_t = \mathcal{G}_{\min} + \frac{\mathcal{G}_{\max} - \mathcal{G}_{\min}}{4}. \tag{10}$$

Then, the coordinates of the centroid of all pixels brighter than $\mathcal{G}_t$ can be estimated as the "center of mass" of a lumped-mass model,

$$r_b = \frac{\sum_i \mathcal{I}_i \, r_i}{\sum_i \mathcal{I}_i} \qquad \text{and} \qquad c_b = \frac{\sum_i \mathcal{I}_i \, c_i}{\sum_i \mathcal{I}_i},$$

where $[r_i, c_i]$ are the coordinates of a generic pixel, $\mathcal{I}_i$ is the lumped-mass binary value, and the index i spans all pixels of the selection box. Similarly, the selected box inertia tensor is

$$\mathcal{T} = \begin{bmatrix} \sum_i \mathcal{I}_i \, (r_i - r_b)^2 & -\sum_i \mathcal{I}_i \, (r_i - r_b)(c_i - c_b) \\ -\sum_i \mathcal{I}_i \, (r_i - r_b)(c_i - c_b) & \sum_i \mathcal{I}_i \, (c_i - c_b)^2 \end{bmatrix}. \tag{11}$$

The greatest positive eigenvalue of $\mathcal{T}$, $\lambda_{\max}$, allows to compute the inclination (ϑ_{sym}) of the axis of symmetry of the illuminated area,

$$\vartheta_{\text{sym}} = \text{atan2}(\hat{\boldsymbol{w}}_{\max}(1), \hat{\boldsymbol{w}}_{\max}(2)),$$

where $\hat{\boldsymbol{w}}_{\max}$ is the eigenvector associated with $\lambda_{\max}$.

Finally, the axis of symmetry is the line passing through $[r_b, c_b]$ with slope $m = \tan \vartheta_{\text{sym}}$. Moreover, the ratio between the eigenvalues provides a measure, albeit approximated, of how much of the target's surface is illuminated: a ratio close to 0 indicates a body barely illuminated while a ratio close to 1 indicates an almost full illuminated body. This ratio provides the admissible range of illumination for the proposed image processing approach. Using the estimated axis of symmetry, a set of parallel axes can be drawn (see Fig. 7) and two set of points are selected; one belongs to the body limb and the other to the terminator. Using Taubin's approach [15] these two sets of points give two circle estimates. The solution with smaller residuals is taken as first estimate of the body center and radius.

To obtain more accurate estimates of the body center and radius, nonlinear least-squares with two-dimensional circular (Moon) and elliptical (Earth) sigmoid functions are adopted. These two sigmoid functions belong to the class of functions described in the following section.

V. Sigmoid functions

Sigmoid functions (SFs) are a class of mathematical functions, which are here used to model the smooth illumination transition around the body limb. To this purpose, one-dimensional linear and two dimensional circular and elliptical SFs are introduced. Each of these functions is defined by a set of parameters, determining the sharpness of the transition (k), the two levels to be connected ($y_{\max}, y_{\min}$), and the location where the transition occurs. These parameters are then estimated by a nonlinear least-squares approach.

A. Linear sigmoid function

A linear sigmoid function (LSF), also called the sigmoidal curve or logistic function, is described by

$$f = y_{\max} + \frac{y_{\min} - y_{\max}}{1 + e^{k(x_t - x)}}, \tag{12}$$

where x_t indicates where the transition occurs and k how rapid the transition is. The higher the value of k the shorter the step transition is. Sample sigmoid functions are plotted in Fig. 5 for $k = [0.1, 0.9]$, $y_{\min} = 20$, $y_{\max} = 150$, and $x_t = 50$.
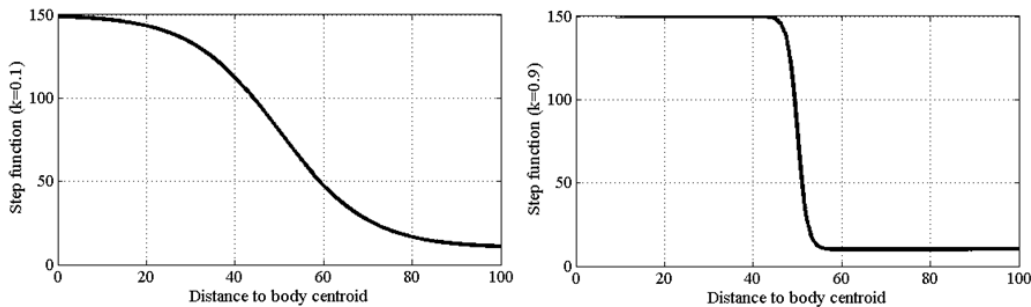

Fig. 5 Examples of Linear Sigmoid Functions

Least-squares with a LSF requires building a Jacobian, an $n \times 4$ matrix, where n is the number of data points, associated with the four unknowns, x_t, $y_{\max}$, $y_{\min}$, and k. By setting

$$\alpha_i = e^{k(x_t - x_i)}, \tag{13}$$

the Jacobian has the form

$$
\mathcal{J} = \begin{bmatrix} \dfrac{\partial f_1}{\partial x_t} & \dfrac{\partial f_1}{\partial y_{\max}} & \dfrac{\partial f_1}{\partial y_{\min}} & \dfrac{\partial f_1}{\partial k} \\[2mm] \vdots & \vdots & \vdots & \vdots \\[2mm] \dfrac{\partial f_n}{\partial x_t} & \dfrac{\partial f_n}{\partial y_{\max}} & \dfrac{\partial f_n}{\partial y_{\min}} & \dfrac{\partial f_n}{\partial k} \end{bmatrix} \tag{14}
$$

where

$$
\begin{aligned}
\frac{\partial f_i}{\partial y_{\min}} &= \frac{1}{1+\alpha_i}, \\
\frac{\partial f_i}{\partial y_{\max}} &= \frac{\alpha_i}{1+\alpha_i} = \alpha_i \frac{\partial f_i}{\partial y_{\min}}, \\
\frac{\partial f_i}{\partial x_t} &= -\frac{(y_{\min}-y_{\max})\alpha_i\,k}{(1+\alpha_i)^2} = -\frac{\partial f_i}{\partial y_{\min}}\frac{\partial f_i}{\partial y_{\max}}(y_{\min}-y_{\max})\,k, \quad \text{and} \\
\frac{\partial f_i}{\partial k} &= -\frac{(y_{\min}-y_{\max})\alpha_i}{(1+\alpha_i)^2}(x_t - x_i) = \frac{(x_t-x_i)}{k}\frac{\partial f_i}{\partial x_t}.
\end{aligned}
$$

The iterative least-squares approach allows the update

$$
\begin{Bmatrix} \Delta x_t \\[2mm] \Delta y_{\max} \\[2mm] \Delta y_{\min} \\[2mm] \Delta k \end{Bmatrix} = (\mathcal{J}^\mathsf{T}\mathcal{J})^{-1}\,\mathcal{J}^\mathsf{T} \begin{Bmatrix} f_1 - f(x_1) \\[2mm] \vdots \\[2mm] f_n - f(x_n) \end{Bmatrix}. \tag{15}
$$

The initial values for $y_{\max}$ and $y_{\min}$ are obtained by averaging a set of first and last data because they depend on the camera exposure time while the initial values for k and x_t are obtained by correlating their values obtained on test images (real, synthetic) with the body type and estimated radius.

B. Circular sigmoid function

Equation (12) can be extended to two-dimensional space with radial distribution

$$
f = y_{\max} + \frac{y_{\min}-y_{\max}}{1+e^{k(r_e-d)}}, \tag{16}
$$

where $d = \sqrt{(c_0-c)^2 + (r_0-r)^2}$ is the distance (in pixel) from the generic pixel, $[r,c]$, to the estimated center $[r_0, c_0]$, and r_e is the estimated radius. By setting,

$$
\beta_i = \sqrt{(c_0-c_i)^2 + (r_0-r_i)^2} \quad \text{and} \quad \alpha_i = e^{k(r_e-\beta_i)},
$$

the Jacobian requires the computation of the following derivatives

$$
\begin{aligned}
\frac{\partial f_i}{\partial r_0} &= \frac{(y_{\min} - y_{\max})\,\alpha_i}{(1 + \alpha_i)^2}\,k\,\frac{r_0 - r_i}{\beta_i}\\
\frac{\partial f_i}{\partial c_0} &= \frac{(y_{\min} - y_{\max})\,\alpha_i}{(1 + \alpha_i)^2}\,k\,\frac{c_0 - c_i}{\beta_i}\\
\frac{\partial f_i}{\partial r_e} &= -\frac{(y_{\min} - y_{\max})\,\alpha_i}{(1 + \alpha_i)^2}\,k\\
\frac{\partial f_i}{\partial k} &= -\frac{(y_{\min} - y_{\max})\,\alpha_i}{(1 + \alpha_i)^2}\,(r_e - \beta_i)\\
\frac{\partial f_i}{\partial y_{\max}} &= \frac{\alpha_i}{1 + \alpha_i}\\
\frac{\partial f_i}{\partial y_{\min}} &= \frac{1}{1 + \alpha_i}.
\end{aligned}
\tag{17}
$$

Circular SFs are used for high accurate estimation of Moon center and radius.

C. Elliptical sigmoid function

An elliptical SF is associated with an ellipse with semi-axes a and b. These observed semi-axes are actually the a' and b' axes computed using Eq. (8). The equation of an ellipse with respect to its own $[x, y]$ axes is

$$
b^2\,x^2 + a^2\,y^2 = a^2\,b^2.
\tag{18}
$$

By setting $\rho = b/a$, Eq. (18) is now a function of a, only, as ρ can be well estimated using the estimated position and Eq. (9),

$$
\rho^2\,x^2 + y^2 = \rho^2\,a^2.
$$

An elliptical SF is therefore described by

$$
f = y_{\max} + \frac{y_{\min} - y_{\max}}{1 + e^{k(\rho\,a - d)}},
$$

where $d = \sqrt{\rho^2\,x^2 + y^2}$, and the direct and inverse coordinate transformations between $[x, y]$ and $[r, c]$ are provided in Appendix A by Eq. (19) and by Eq. (20), respectively. The ellipse has center $[r_0, c_0]$ and the ellipse is rotated by the angle ϑ (see Fig. 10). These variables, can be estimated using the transformation matrix $C_{ci}C_{ie}$, where C_{ie} moves from elliptical cone to inertial and C_{ci} moves from inertial to camera. In camera coordinate frame, the ellipse center is provided by $\boldsymbol{b}_c = C_{ci}C_{ie}\{0,\,0,\,\pm1\}^{\mathrm{T}}$, and the semi-axes orientation are provided by the directions $\hat{\boldsymbol{b}}_a = C_{ci}C_{ie}\{\pm a',\,0,\,\sqrt{1 - a'^2}\}^{\mathrm{T}}$ and $\hat{\boldsymbol{b}}_b = C_{ci}C_{ie}\{0,\,\pm b',\,\sqrt{1 - b'^2}\}^{\mathrm{T}}$, respectively.

15

By setting

$$\beta_i = \sqrt{\rho^2 x_i^2 + y_i^2} \qquad \text{and} \qquad \alpha_i = e^{k(\rho a - \beta_i)},$$

the Jacobian requires the computation of the following derivatives

$$
\begin{aligned}
\frac{\partial f_i}{\partial r_0} &= \frac{(y_{\min} - y_{\max})\,\alpha_i}{(1+\alpha_i)^2}\, k\, \frac{\rho^2 x_i \sin\vartheta + y_i \cos\vartheta}{\beta_i} \\
\frac{\partial f_i}{\partial c_0} &= \frac{(y_{\min} - y_{\max})\,\alpha_i}{(1+\alpha_i)^2}\, k\, \frac{y_i \sin\vartheta - \rho^2 x_i \cos\vartheta}{\beta_i} \\
\frac{\partial f_i}{\partial a} &= -\frac{(y_{\min} - y_{\max})\,\alpha_i}{(1+\alpha_i)^2}\, k\, \rho \\
\frac{\partial f_i}{\partial \vartheta} &= \frac{(y_{\min} - y_{\max})\,\alpha_i}{(1+\alpha_i)^2}\, k\, \frac{x_i y_i(\rho^2 - 1)}{\beta_i} \\
\frac{\partial f_i}{\partial y_{\max}} &= \frac{\alpha_i}{1+\alpha_i} \\
\frac{\partial f_i}{\partial y_{\min}} &= \frac{1}{1+\alpha_i} \\
\frac{\partial f_i}{\partial k} &= -\frac{(y_{\min} - y_{\max})\alpha_i}{(1+\alpha_i)^2}\,(\rho a - \beta_i).
\end{aligned}
$$

VI.   Example by numerical test

This section provides the numerical results for a real Moon image taken from ground (Houston area) on March 6, 2013 at 06:08:10 CDT. The original image is shown in the top left of Fig. 6. The Moon distance is known with very low precision (some Earth radii). A simple median filter is applied to smooth the image, mainly to identify a single pixel belonging to the Moon. The filter is first applied to remove isolated stars or reflecting S/C or dead or saturated pixels. The brightest pixel is shown in the top-right of Fig. 6 as black dot. Around that pixel a box whose dimension is the observed diameter of the Moon (computed using the approximated Moon distance and the camera parameters) is also shown. This box allows to restrict the image processing to a rectangular subset of the original image, the sub image shown in the bottom-left of Fig. 6. Using the value of the brightest pixel in the filtered image a threshold value, as given in Eq. (10) is computed and used to convert the graytone image to a binary image, as shown in the bottom-right of Fig. 6. Then the eigenanalysis of the binary images, as provided by Eqs. (11) and subsequent, gives a ratio of eigenvalues, $\frac{\lambda_{\min}}{\lambda_{\max}} = 0.107$, a value indicating the illuminated area.

The axis of symmetry (eigenvector associated with the maximum eigenvalue) of the illuminated part is shown in the bottom-right of Fig. 6, together with its orthogonal direction (eigenvector
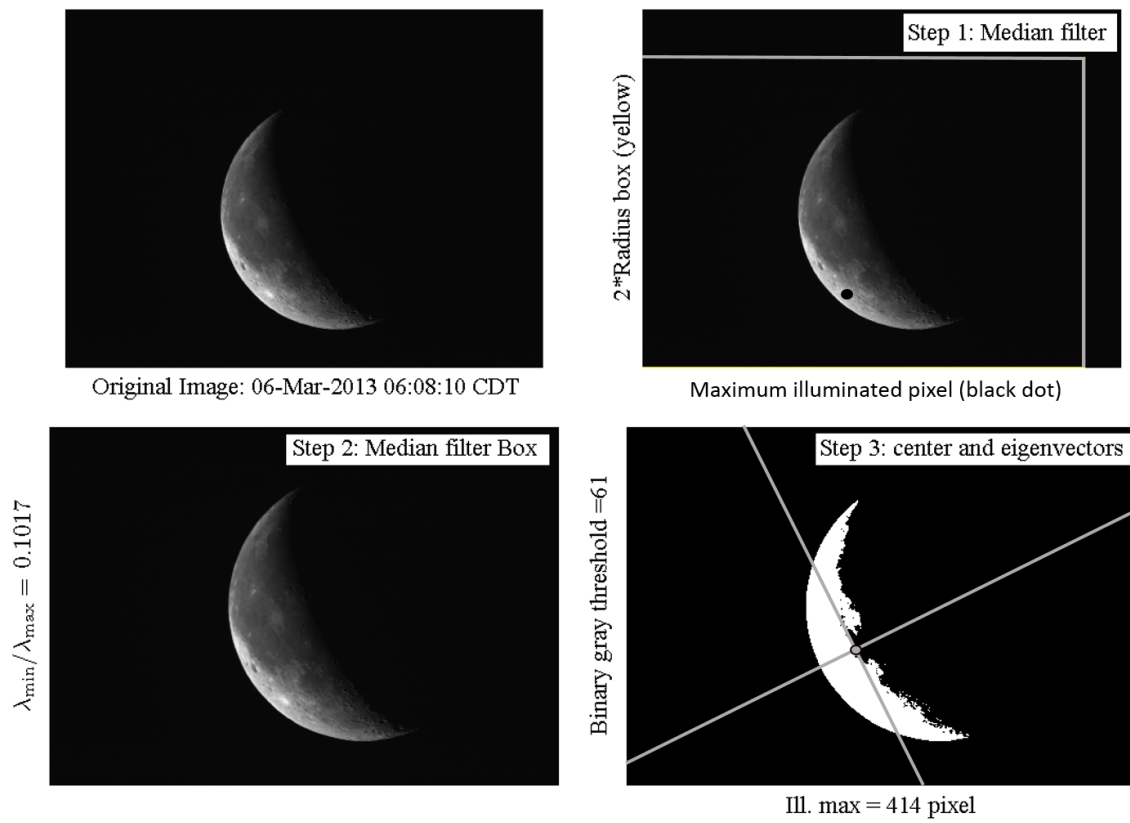
16

Fig. 6 First steps of image processing

associated with the minimum eigenvalue). This axis of symmetry is an approximation of the real symmetric axis of the illuminated area. As shown in Fig. 7, this approximation is useful to identify the set of pixels belonging to the bright limb as well as those pixels belonging to the terminator. The
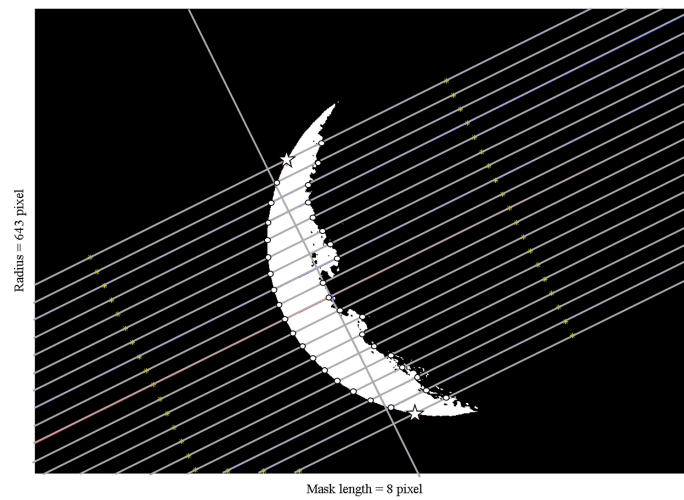

Fig. 7 Selection of bright limb and terminator points

direction of the approximated axis of symmetry is then used to draw a set of lines parallel to the axis of symmetry with constant step size (1/11 of the estimated Moon radius). Along these lines a mask of 8 pixels ([0, 0, 0, 0, 1, 1, 1, 1]) is used to identify the maximum correlation with the two transitions (one associated with the terminator and one with the bright limb) in the binary images. Using these two sets of transition points (19 points each set) two distinct estimations of Moon center and radius are obtained using Taubin's method [15]. The set associated with minimum standard deviation of residuals is identified as the bright limb and the associated estimation of Moon center and radius is used as initial guess for a nonlinear least-squares estimation of these parameters using circular sigmoid function using Eqs. (16) and (17).
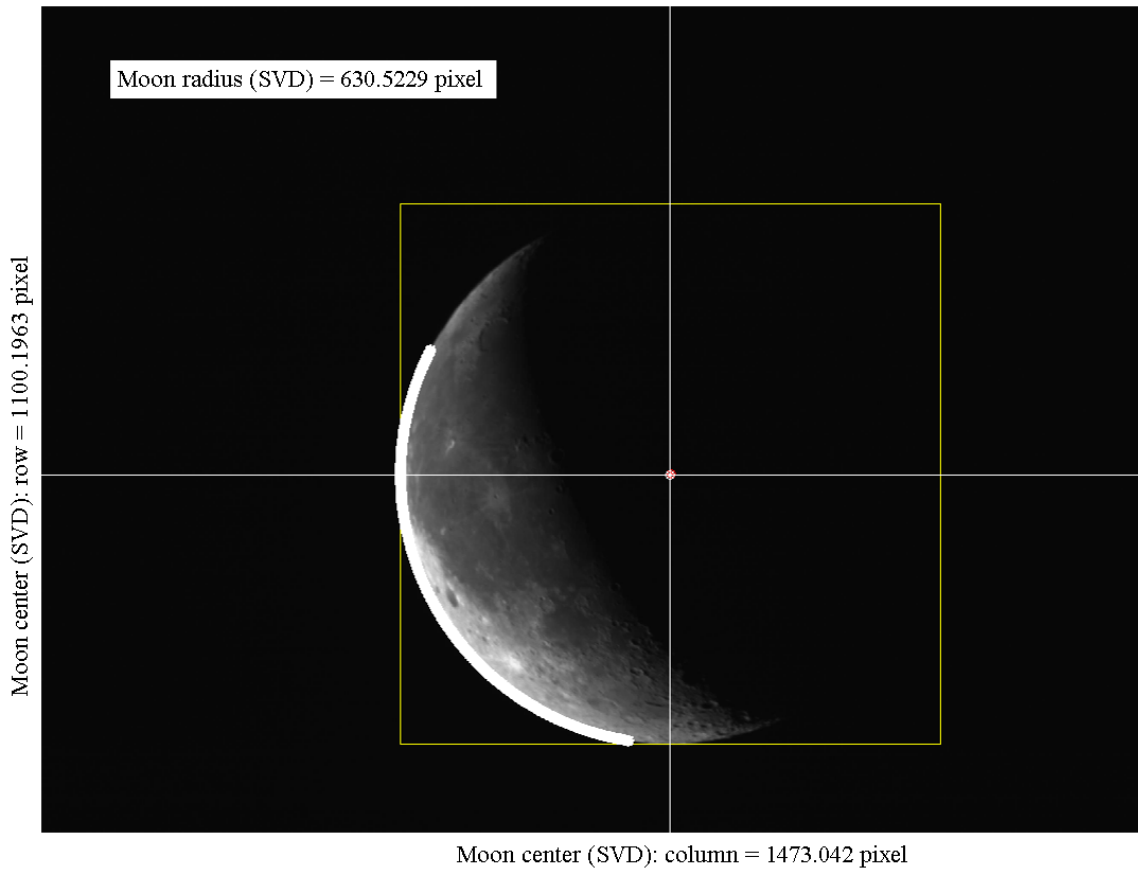
Fig. 8 Results form Least-squares using circular SF

The pixels used in the circular SF least-squares estimate are those between two radii, $\hat{r} \pm \Delta r$, where the values of Δr is a function of the initial Moon radius estimate ($\hat{r}$), and between the two directions from the estimated Moon center to the farthest two pixels (on the Moon bright limb)

from the axis of symmetry (marked by white stars in Fig. 7). All the selected pixels are marked in white in Fig. 8. In this example, the values of $y_{\max}$ and $y_{\min}$ have been set equal to the mean values of the pixels selected using the two extreme radii while the sigmoid transition constant, k, has been set to 3. Note that, by prescribing the values for $y_{\max}$, $y_{\min}$, and k the size of the Jacobian used in the least-squares is reduced from $n \times 6$ to $n \times 3$, where n is the total number of pixels selected. Table 1 shows the convergence step values for this example.

Table 1 Circular SF with $y_{\max} = 132.59266$, $y_{\min} = 26.746643$, and $k = 3$

Iteration	Radius	Row	Column
0	633.51611	1098.0115	1475.7666
1	632.13850	1099.0309	1474.4326
2	631.42484	1099.5501	1473.7903
3	631.04593	1099.8232	1473.4667
4	630.83481	1099.9744	1473.2924
5	630.71164	1100.0622	1473.1927
6	630.63784	1100.1147	1473.1336
7	630.59301	1100.1466	1473.0978
8	630.56560	1100.1660	1473.0760
9	630.54879	1100.1780	1473.0627
10	630.53846	1100.1853	1473.0544
11	630.53211	1100.1898	1473.0494
12	630.52821	1100.1925	1473.0463
13	630.52581	1100.1942	1473.0444
14	630.52434	1100.1953	1473.0432
15	630.52343	1100.1959	1473.0425
16	630.52287	1100.1963	1473.0420

Using the attitude provided by star tracker, the Observer-to-Moon vector is then estimated in J2000 and, by subtracting the Moon vector position, the observer position is finally estimated.

As a final side note, a rough estimate of the camera attitude can be obtained. In fact, the estimated direction to the Moon center and the axis of symmetry are two directions identifying the

plane where the Moon, the Sun, and the observer are. This means that, by looking at the Moon (or Earth), two directions can be estimated in body and inertial reference frames. Therefore, it is possible to estimate the camera attitude using a single-point attitude estimation technique (See Refs. [16, 17]). These two directions are observed with different accuracy and, consequently, the attitude can be estimated using any single-point weighted attitude determination algorithm. In general, the direction to the Moon center is more accurate than the axis of symmetry which is affected by the variations of the surface topology (Moon) or by the distribution of high-altitude clouds (Earth). For the image under consideration the direction cosine matrix of the camera attitude (moving from inertial to Camera frames) is

$$
C_{ci} = \begin{bmatrix} -0.88135 & -0.25746 & 0.39615 \\ -0.45769 & 0.25723 & -0.85109 \\ 0.11722 & -0.93142 & -0.34455 \end{bmatrix}.
$$

VII. Conclusions

This paper introduces a novel algorithm and the associated mathematical theory developed to process images of the Earth of Moon for autonomous, onboard navigation in cislunar space. While a multitude of image processing and limb detection algorithms exist, this work focuses on a simple and robust algorithm able to produce good navigation results onboard a spacecraft subject to the computational limitation of a flight computer. The processed images can be taken by a visible CCD or CMOS camera and the data extracted by the algorithm are the direction to the body center and either the body radius, for the Moon, or greatest semi-major axis, for the Earth. The provided data can be used by an estimation algorithm, such as an extended Kalman filter, to provide a navigation solution.

Novelties of the algorithm include the use of Circular and Elliptical Sigmoid functions in a least-squares algorithm. The equation of an observed triaxial ellipsoid is shown to be described by an ellipse as a projection of the curve obtained by intersecting an elliptic cone with a sphere, and the equation of the terminator is provided for the generic triaxial ellipsoid. These features of the proposed method allow the algorithm to produce highly accurate measurements of the direction and apparent size of the Earth and Moon. It is shown that the direction to the center of the observed

ellipse and the direction of the body center are displaced by an offset. The procedure showing how to take into account this offset is provided in order to improve the estimate of the spacecraft position.

A numerical example of the image processing algorithm using an actual photograph of the Moon is shown, and demonstrates that the algorithm is a good option for autonomous cislunar navigation under the conditions of this analysis.

Acknowledgments

References

[1] D'Souza, C., Crain, T., and Clark, F.C. "Spacecraft Cislunar Guidance and Navigation," AIAA Guidance Navigation and Control Conference, AIAA-07-6681, Hilton Head, S.C., August 20–23, 2007.

[2] Battin, R.H. *An Introduction to the Mathematics and Methods of Astrodynamics*, AIAA Education Series, American Institude of Aeronautics and Astronautics, New York, NY, 1987.

[3] Tuckness, D.G. and Young, S.Y. "Autonomous Navigation for Lunar Transfer," AIAA *Journal of Spacecraft and Rockets*, Vol. 32, No. 2, March-April 1995, pp. 279–285.

[4] Zanetti, R. "Autonomous Midcourse Navigation for Lunar Return," AIAA *Journal of Spacecraft and Rockets*, 46(4): 865–873, July–August 2009.

[5] Chorym, M.A., Hoffman, D.P., Major, C.S., and Spector, V.A. "Autonomous Navigation - Where we are in 1984," *Guidance and Control*, Keyston CO, 1984, 27–37.

[6] Christian, J.A. and Lightsey, E.G. "Onboard Image-Processing Algorithm for a Spacecraft Optical Navigation Sensor System," *Journal of Spacecraft and Rockets*, 2012, *49(2)*, 337–352.

[7] Owen, W., Duxbury, T., Acton, C., Synnott, S., Riedel, J., and Bhaskaran, S. "A Brief History of Optical Navigation at JPL," AAS Guidance and Control Conference, AAS 08-053, 2008.

[8] Synnott, S., Donegan, A., Riedel, J., and Stuve, J. "Interplanetary Optical Navigation: Voyager Uranus Encounter," AIAA Astrodynamics Conference, AIAA Paper 1986–2113, 1986.

[9] Riedel, J.E., Owen, W.M. Jr., Stuve, J.A., Synnott, A.P., and Vaughan, R.A. "Optical Navigation During the Voyager Neptune Encounter," AIAA/AAS Astrodynamics Conference, AIAA Paper 1990–2877, 1990.

[10] Gillam, S.D., Owen, W.M. Jr., Vaughan, A.T., Wang, T.C.M., Costello, J.D., Jacobson, R.A., Bluhm, D., Pojman, J.L., and Ionasescu, R. "Optical Navigation for the Cassini/Huygens Mission," AIAA/AAS Astrodynamics Specialist Conference. Mackinac Island, MI, USA, 2007.

[11] Li, S., Lu, R., Zhang, L., and Peng, Y. "Image Processing Algorithms For Deep-Space Autonomous Optical Navigation," *Journal of Navigation*, 2013, *66(4)*, 605–623.

[12] Christian, J.A. "Optical Navigation Using Planet's Centroid and Apparent Diameter in Image," *Journal of Guidance, Control, and Dynamics*, 2015, *38(2)*, 192–204.

[13] Mortari, D., de Dilectis, F., and D'Souza, C. "Image Processing of Illuminated Ellipsoid," AAS 13–853, 2013 AAS/AIAA Astrodynamics Specialist Conference, Hilton Head, SC, August 11–15, 2013.

[14] `http://naif.jpl.nasa.gov/naif/toolkit.html` "NAIF. The Navigation and Ancillary Information Facility," *The SPICE Toolkit*, NASA-JPL.

[15] Taubin, G. "Estimation of Planar Curves, Surfaces, and Nonplanar Space Curves Defined by Implicit Equations with Applications to Edge and Range Image Segmentation," *IEEE Transactions on Pattern Analysis and Machine Intelligence*, Vol. 13, No. 11, November 1991.

[16] Mortari, D. "Moon-Sun Attitude Sensor," AIAA *Journal of Spacecraft and Rockets*, Vol. 34, No. 3, May–June 1997, pp. 360–364.

[17] Park, K.J. and Mortari, D. "Planet or Moon Image Processing for Spacecraft Attitude Estimation," *Journal of Electronic Imaging*, Vol. 17, No. 2, April–June 2008, pp. 1–11.

Appendix I: Reference frames and coordinates transformations

The proposed image processing requires the use of several reference frames. These are:

- $[\hat{\boldsymbol{i}}_1, \hat{\boldsymbol{i}}_2, \hat{\boldsymbol{i}}_3]$ Earth-centered Inertial (J2000 or ICRF) reference frame.

- $[\hat{\boldsymbol{o}}_1, \hat{\boldsymbol{o}}_2, \hat{\boldsymbol{o}}_3]$ Spacecraft principal axes reference frame.

- $[\hat{\boldsymbol{b}}_1, \hat{\boldsymbol{b}}_2, \hat{\boldsymbol{b}}_3]$ Observed body-centered body-fixed reference frame (Earth or Moon).

- $[\hat{\boldsymbol{c}}_1, \hat{\boldsymbol{c}}_2, \hat{\boldsymbol{c}}_3]$ Camera reference frame. $\hat{\boldsymbol{c}}_1$ and $\hat{\boldsymbol{c}}_2$ axes lie on the camera imager while $\hat{\boldsymbol{c}}_3$-axis is pointing from imager center to the lens.

- $[\hat{\boldsymbol{w}}_1, \hat{\boldsymbol{w}}_2, \hat{\boldsymbol{w}}_3]$ Elliptical cone reference frame, as provided by Eq. (7).

To move from/to five different reference frames four coordinates transformations are needed. The direction cosine matrices of these transformations are defined in Table 2.
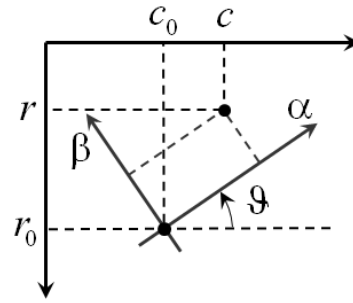
Table 2 Coordinates transformation

Inertial → Spacecraft	$\hat{\boldsymbol{o}} = C_{oi}\,\hat{\boldsymbol{\imath}}$
Inertial → Observed Body	$\hat{\boldsymbol{b}} = C_{bi}\,\hat{\boldsymbol{\imath}}$
Spacecraft → Camera	$\hat{\boldsymbol{c}} = C_{co}\,\hat{\boldsymbol{o}}$
Observed Body → Elliptical cone	$\hat{\boldsymbol{w}} = C_{wb}\,\hat{\boldsymbol{b}}$

In addition to the previous reference frames, the transformations between imager coordinates ($[r,c]$ or $[x,y]$) and unit vectors ($\boldsymbol{c}$) are given (see Fig. 9). These transformations are those of pin-hole camera model.
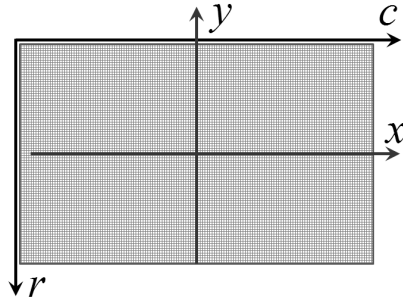
Fig. 9 $[r,c]$ **and** $[x,y]$ **reference frames**   **Fig. 10** $[r,c]$ **and** $[\alpha,\beta]$ **reference frames**

In the case the optical axis coincides with the center of the detector (no optical axis offset), the direct transformations from $\boldsymbol{c}$ to $[x,y]$ are,

$$x = -f\,\frac{\hat{\boldsymbol{c}}(1)}{\hat{\boldsymbol{c}}(3)} \qquad \text{and} \qquad y = -f\,\frac{\hat{\boldsymbol{c}}(2)}{\hat{\boldsymbol{c}}(3)},$$

where coordinates, x and y, and focal length, f, are provided in mm. The inverse transformation is

$$\hat{\boldsymbol{c}} = \frac{1}{\sqrt{x^2 + y^2 + f^2}}\,\{-x,\ -y,\ f\}^{\mathrm{T}}.$$

The transformations from $[x,y]$ to $[r,c]$ coordinates are,

$$r = \frac{n_r + 1}{2} - \frac{y}{d_r} \qquad \text{and} \qquad c = \frac{n_c + 1}{2} + \frac{x}{d_c}, \tag{19}$$

where d_r and d_c are row and column pixel pitch [mm]. The inverse transformations are

$$x = d_c\left(c - \frac{n_c + 1}{2}\right) \qquad \text{and} \qquad y = d_r\left(\frac{n_r + 1}{2} - r\right). \tag{20}$$

APPENDIX II: Terminator equation

This appendix provides the equation of the terminator in the camera reference frame. The canonical equation of an ellipsoid (in the observed body reference frame) is provided by Eq. (1). Let $\hat{\boldsymbol{v}}_s$ be the Sun rays direction (unit vector) in the body reference frame. This vector can be computed from the known epoch and attitude. The vector,

$$\boldsymbol{p} = \boldsymbol{x} + t\,\hat{\boldsymbol{v}}_s,$$

intersects the ellipsoid if $\boldsymbol{p}$ satisfies Eq. (1), $\boldsymbol{p}^{\mathrm{T}} J \boldsymbol{p} = 1$, or equivalently,

$$2t\,\hat{\boldsymbol{v}}_s^{\mathrm{T}} J \boldsymbol{x} + t^2\,\hat{\boldsymbol{v}}_s^{\mathrm{T}} J \hat{\boldsymbol{v}}_s = 0.$$

This equation has a trivial solution, $t_1 = 0$, and the solution $t_2 = -2\dfrac{\hat{\boldsymbol{v}}_s^{\mathrm{T}} J \boldsymbol{x}}{\hat{\boldsymbol{v}}_s^{\mathrm{T}} J \hat{\boldsymbol{v}}_s}$. Enforcing $t_2 = 0$, once again the two solutions coincide and hence the locations where the Sun rays are tangent to the ellipsoid are obtained. This implies, $\hat{\boldsymbol{v}}_s^{\mathrm{T}} J \boldsymbol{x} = 0$. Therefore, the terminator equation is described by

$$\hat{\boldsymbol{v}}_s^{\mathrm{T}} J\,\boldsymbol{x} = 0 \qquad \text{subject to} \qquad \boldsymbol{x}^{\mathrm{T}} J\,\boldsymbol{x} = 1. \tag{21}$$

By setting,

$$\boldsymbol{w}_s = \sqrt{J}\,\hat{\boldsymbol{v}}_s = \left\{ \frac{v_{s1}}{a},\ \frac{v_{s2}}{b},\ \frac{v_{s3}}{c} \right\}^{\mathrm{T}} \qquad \text{and} \qquad \boldsymbol{y} = \sqrt{J}\,\boldsymbol{x} = \left\{ \frac{x_1}{a},\ \frac{x_2}{b},\ \frac{x_3}{c} \right\}^{\mathrm{T}},$$

Eq. (21) becomes

$$\boldsymbol{w}_s^{\mathrm{T}}\,\boldsymbol{y} = 0 \qquad \text{subject to} \qquad \boldsymbol{y}^{\mathrm{T}}\,\boldsymbol{y} = 1.$$

This implies that the solution, $\boldsymbol{y}$, is a unit vector ($\boldsymbol{y} = \hat{\boldsymbol{y}}$) orthogonal to $\boldsymbol{w}_s$. By setting,

$$\hat{\boldsymbol{y}} = \{\cos\varphi \cos\vartheta,\ \sin\varphi \cos\vartheta,\ \sin\vartheta\}^{\mathrm{T}},$$

the equation

$$\frac{v_{s1}}{a} \cos\varphi \cos\vartheta + \frac{v_{s2}}{b} \sin\varphi \cos\vartheta + \frac{v_{s3}}{c} \sin\vartheta = 0$$

that can be re-arranged as,

$$\tan\vartheta = -\frac{c\,v_{s1}}{a\,v_{s3}} \cos\varphi - \frac{c\,v_{s2}}{b\,v_{s3}} \sin\varphi. \tag{22}$$

By varying φ between 0 and 2π, Eq. (22) allows to compute to corresponding value for ϑ. Therefore, the $\boldsymbol{x}$ vector in the body-fixed reference frame is given by

$$\boldsymbol{x} = \left(\sqrt{J}\right)^{-1} \hat{\boldsymbol{y}} = \{a \cos\varphi \cos\vartheta, \ b \sin\varphi \cos\vartheta, \ c \sin\vartheta\}^{\mathrm{T}}.$$

Finally, the terminator in the camera reference frame, $\boldsymbol{t}_{\mathrm{c}}$, is provided by,

$$\boldsymbol{t}_{\mathrm{c}} = C_{ci}\, C_{ib}\, (\boldsymbol{x} - \boldsymbol{P}_0),$$

where $\boldsymbol{P}_0$ is the camera position vector in the body-fixed reference frame and the product $C_{ci}\, C_{ib}$ is the transformation matrix moving from body to camera reference frames.